Stabilization of phase-pure rhombohedral $HfZrO_4$ in pulsed laser deposited thin films

Laura Bégon-Lours,[1,*] Martijn Mulder,[1] Pavan Nukala,[2] Sytze de Graaf,[2] Yorick A. Birkhölzer,[1] Bart Kooi,[2] Beatriz Noheda,[2] Gertjan Koster,[1] and Guus Rijnders[1]

[1]Inorganic Materials Science, University of Twente, 7500 AE, Netherlands
[2]Zernike Institute of Advanced Materials, University of Groningen, 9747 AG, Netherlands

(Received 11 December 2019; accepted 6 March 2020; published 7 April 2020)

Controlling the crystalline structure of hafnium zirconate and its epitaxial relationship to a semiconducting electrode has high technological interest, as ferroelectric materials are key ingredients for emerging electronic devices. Using pulsed laser deposition, a phase-pure, ultrathin film of $HfZrO_4$ is grown epitaxially on a GaN(0001)/Si(111) template. Since standard microscopy techniques do not allow us to determine with certitude the crystalline structure of the film due to the weak scattering of oxygen, differentiated differential phase contrast scanning transmission electron microscopy is used to allow the direct imaging of oxygen columns in the film. Combined with x-ray diffraction analysis, the polar nature and rhombohedral *R*3 symmetry of the film are demonstrated.

DOI: 10.1103/PhysRevMaterials.4.043401

I. INTRODUCTION

The integration of ferroelectric materials on semiconductors paves the way to the development of novel technologies based on the combination of functionalities of two different materials systems. First, GaN-based high electron mobility transistors (HEMTs) for high-power electronics show excellent performance thanks to a wide band gap and high electron drift velocity. The use of a ferroelectric gate further increases the performance (i.e., by increasing the threshold voltage or the ON/OFF ratio) of such transistors [1–3]. However, the integration of such ferroelectric materials (usually perovskites [2,4–7]) on GaN is challenging due to the large lattice mismatch between the two structures, and a buffer layer, such as MgO [2,7], Al_2O_3 [6], or TiO_2 [8] is commonly used to allow for the mismatch. Direct integration of a fully epitaxial ferroelectric material on GaN is the promise of further improvement for such devices. Furthermore, the remanence and electric field control of the polarization makes ferroelectric materials ideal candidates for nonvolatile memories and in-memory computing [9]. Specifically, HfO_2-based ferroelectric structures on silicon [10] or transparent conducting oxides [11] show excellent memristive behaviors and low-voltage operation thanks to its high dielectric constant. Layers of doped-hafnium have been extensively studied since 2011, when a ferroelectric phase of this common dielectric material was first discovered [12] in films synthesized by atomic layer deposition (ALD). These films exhibited ferroelectricity only at the nanoscale, and metastable polar polymorphs were established to be responsible for this behavior. The lowest-energy orthorhombic (o-) phase was widely observed in many studies. The exploration of the conditions and mechanisms to obtain the o phase is ongoing, in particular the role and the nature of the top and bottom electrodes: epitaxial strain [13], mechanical strain [14], oxidation of the electrode [15,16], the composition of the film [15,17–19], and the thermal annealing conditions [20–22]. ALD, however, always results in polycrystalline films, with an overall polarization smaller compared to the polarization of single grains, in addition to the need of a wake-up process. Other techniques such as sputtering [23], metal-organic chemical-vapor deposition (MOCVD) [24] (including on GaN [1]), or chemical solution deposition (CSD) [25] have been explored, similarly resulting in polycrystalline films. On the contrary, pulsed laser deposition (PLD) is a vapor phase technique that allows the direct epitaxial growth of thin films. It has been recently used for the fabrication of $HfZrO_4$ (HZO) thin films on perovskite electrodes [26–29], and structural analysis of films grown on $La_{0.7}Sr_{0.3}MnO_3/SrTiO_3$ (LSMO/STO) (001) substrates demonstrated the occurrence of a unique phase with rhombohedral (r) symmetry [26].

The r and o phases had in common that they only occurred for film thickness below 10–15 nm [21,26]. As the thickness of the film increased, the fraction of grains crystallizing in the bulk monoclinic phase increased, limiting the applications requiring ferroelectricity. Despite *ab initio* studies of HfO_2 with several dopants [30], it is still unclear what conditions led to the stabilization of which polar phase, pointing to the need for the systematic study of high-quality films under various conditions (substrates, orientation, etc.). As the thickness of the film decreased (below ∼5 nm), the ferroelectricity vanished [31,32], either because of a depolarizing field at the interface with the electrodes [33,34], or because of an interfacial layer in a different phase [26]. Controlling the formation of ferroelectric phases of hafnium zirconate is necessary for the fabrication of novel nonvolatile memories, as it is a candidate for the fabrication of negative capacitance transistors [35], ferroelectric field-effect transistors [36–39], or ferroelectric tunnel junction [31,40] devices.

In this context, here we explore the epitaxial growth of HZO by pulsed laser deposition on a template with a

*l.c.y.begon-lours@utwente.nl

 ©2020 American Physical Society

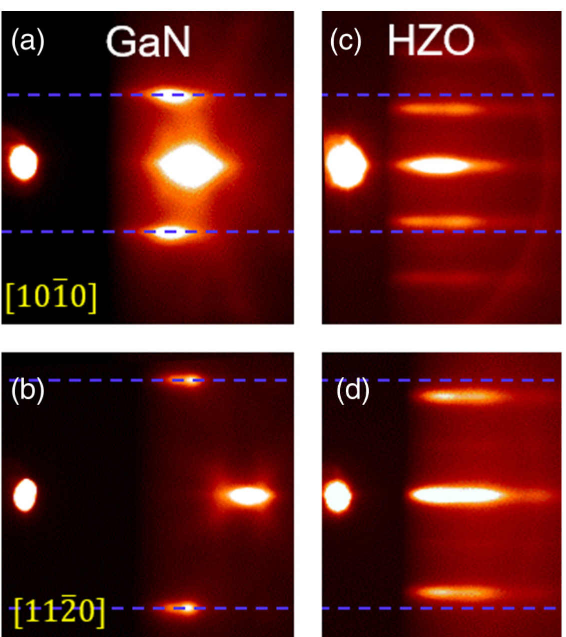

FIG. 1. RHEED diffraction patterns of GaN (a), (b) and HZO (c), (d) along the [10–10] direction of GaN (a), (c) and along the [11–20] (b), (d), showing the epitaxy of HZO on GaN. The blue lines are guides to the eye.

trigonal symmetry, gallium nitride buffered Si [GaN (0001)]. In this research, using reflection high-energy electron diffraction (RHEED), x-ray diffraction (XRD) and aberration corrected scanning transmission electron microscopy (STEM), we will show that the HZO film crystallized in a rhombohedral symmetry, is phase pure and is [111] oriented. Fundamentally, this is a demonstration of a pure r phase on a nonperovskite substrate and provides more clues to its preferential stabilization. From an application standpoint, our work demonstrates that the oriented polar r phase can be seamlessly integrated onto Si-based substrates.

II. RESULTS

A. Epitaxy of the $HfZrO_4$ film on GaN

We first analyze the growth mode during the deposition. First, the main diffraction peaks in the reflection high-energy electron diffraction (RHEED) pattern of the GaN substrate and the azimuthal angles are measured, as shown in Figs. 1(a) and 1(b). The substrate is then heated, and the intensity of the main diffraction peak is monitored during the growth. It shows a drop in intensity in the very early stage of the deposition, followed by a recovery as the thickness of the film increases. In addition, the morphology of the film reproduces the features (terraces) of the GaN template (an atomic force microscopy image can be found in Fig. S1 in the Supplemental Material [41]), which is indicative of a steady-state (or step-flow-like) growth mode for the HZO film. Undoped GaN films were chosen as a template to allow for an atomically flat surface with no defects. After the deposition and cooling down, photographs of HZO diffraction patterns are taken. We observe that films of 3–11 nm present very similar patterns with comparable *d* spacings, indicating homogeneous growth. The homogeneity of the film after cooling down is confirmed by energy dispersive x-ray (EDX) mapping of the chemical elements in the film (see Fig. S2 [41]). The RHEED patterns of the film show a single-crystalline phase, with a sixfold symmetry. Figure 1 compares RHEED patterns of the HZO film (c), (d) and of the GaN substrate (a), (b): despite the large lattice mismatch (14%) the main symmetry axes are found at the same azimuthal angles as the main diffraction axes [10$\bar{1}$0] and [11$\bar{2}$0] of the GaN template, demonstrating an epitaxial relationship between the film and the substrate.

B. Determination of a polar, rhombohedral phase of HZO

Standard x-ray diffraction (XRD) analysis was carried out on the HZO film. The thickness of the HZO film was determined to be 58.3 Å $\approx 20 \times 2.96$ Å by x-ray reflectometry. Symmetric scans were carried out around the Si (222) peak of the substrate, shown in Fig. 2(a). The GaN epitaxial film signature consists of three peaks for the (0001) reflection. The peaks at $2\theta = 30.20^\circ$ (plain arrow) and $2\theta = 32.30^\circ$ (dashed arrow) originate from the HZO film. The out-of-plane lattice parameter associated with the peak at $2\theta = 30.20^\circ$ is 2.96 Å. Thus, the position of the feature at $2\theta = 32.30^\circ$ matches the expected position for a Laue fringe [42] of 20 diffracting planes separated by 2.96 Å, confirming that the film is highly oriented and structurally perfect. The inset of Fig. 2(a) shows the rocking curve around the HZO peak, showing a full width at half maximum of 0.26°. Note that in the literature, a strong peak at $2\theta = 30.20^\circ$ is generally attributed to either the orthorhombic or the tetragonal phase of HZO but further analysis below will show it is also compatible with the rhombohedral phase. Even though o/t phases are more favorable thermodynamically than the rhombohedral phases in bulk, PLD allows for the stabilization of other phases because of two possible mechanisms: (1) as PLD is an off-equilibrium deposition technique, this phase might be kinetically stabilized (note that also the oxygen pressure and the temperature are important parameters). (2) Because of the symmetry of the substrate and chemical termination of the substrate, the orthorhombic phase might be stabilized by favorable interface energies. Currently, we cannot determine which mechanism is leading; this needs further research.

Figure 2(b) shows pole figure of the HZO film taken at a tilt of $\chi \approx 71^\circ$. It reveals six peaks separated in φ by 60°. This is consistent with the existence of two domains (D1 comprising P1–P3 and D2 comprising P4–P6) rotated by 180° with respect to the [111] growth axis. In comparison, the pole figure of the GaN/Si substrate only shows three poles, consistent with the trigonal symmetry of GaN(0001) and Si(111). Figure 2(c) shows symmetric scans taken at these poles. Scans across P1–P3 (belonging to one domain), show a peak at $2\theta = 30.45^\circ$ whereas the out-of-plane diffraction peak was at $2\theta = 30.20^\circ$. Such a 3:1 multiplicity is a strong signature of a rhombohedral space group.

We then analyzed the local structure of our films using scanning transmission electron microscopy (STEM) imaging. High-angle annular dark-field (HAADF)–STEM images were taken from the cross section of the film, revealing a homogeneous film with two types of domains [labeled R1 and R2 in Fig. 3(a)] Local fast Fourier transforms of the image

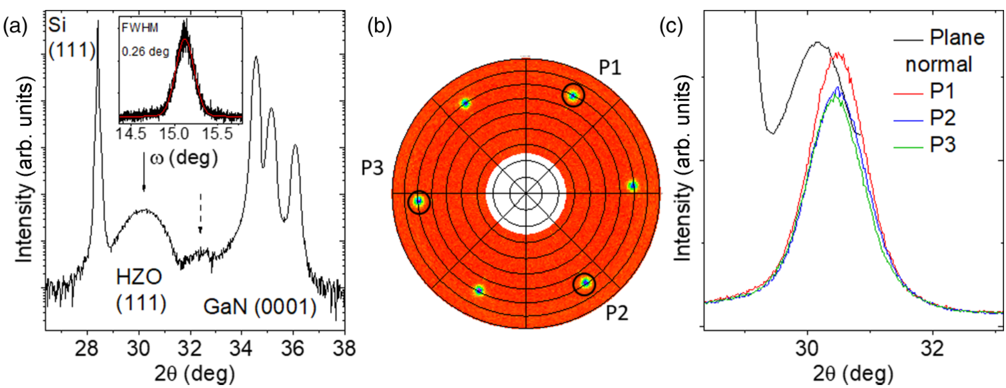

FIG. 2. (a) Symmetric XRD scan of a $HfZrO_4$ film with a thickness of 5.9 nm. The plain arrow indicates the HZO (111) diffraction peak and the dashed arrow a satellite Laue fringe. The inset shows a rocking curve around the HZO diffraction peak. (b) Pole figures of the same film with six peaks at $\chi \approx 71^\circ$ labeled P1–P6. (c) Black: symmetric XRD scans of the 111 peak, red, blue, green: GIXRD scans of peaks P2, P4, P6.

[Figs. 3(b) and 3(c)] show that the domains are (111) oriented, and are rotated 180° with respect to the [111] direction, consistent with our pole figure analysis. The corresponding plane spacings measured by XRD are $d_{111} = 2.96$ Å and $d_{1\text{-}11} = 2.93$ Å (error: ±0.02 Å). Closer analysis of the images indicates that the R grains relax close to the surface. The d spacings from STEM analysis are listed in Table I.

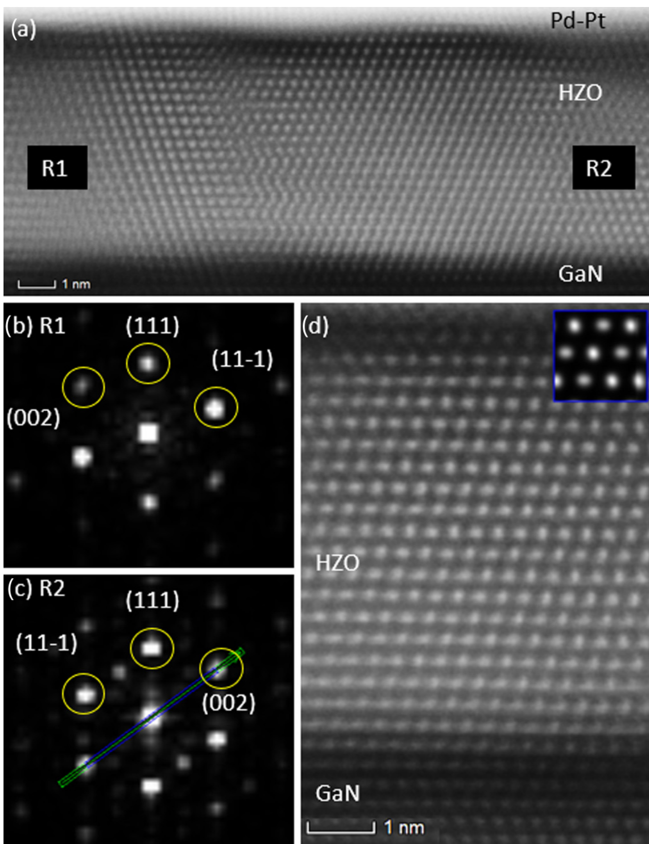

FIG. 3. (a) Cross-sectional HAADF-STEM image of a 5.9-nm $HfZrO_2$ sample. The different layers are labeled with their respective material. In the HZO layer, the R1 and R2 domains have been indicated. (b), (c) show the Fourier transforms of the R1 and R2 domains, in which the diffraction spots are labeled. (d) HAADF-STEM image of a R2 domain. The inset shows the simulated HAADF image for the r phase.

The HAADF image shown in Fig. 3(d) from a single domain shows alternating contrast in the cationic columns along the ⟨112⟩ in plane. This is consistent with our multislice HAADF simulations of $R3$ and $R3m$ phases (and not the o phase) obtained at a sample thickness of 20 nm (see inset). Thus, comparing HAADF simulations of known HZO phases to the experimental data confirms the rhombohedral symmetry of the lattice.

To further determine the precise symmetry of the r phase, we performed oxygen column imaging via differential phase contrast (DPC) STEM, as shown in Figs. 4(a) and 4(b). The DPC STEM technique uses a segmented annular detector to measure the center of mass (COM) of the ronchigram at every probe position. Since the COM is linear with the in-plane electric field, the DPC images represent the projected in-plane electric field of the specimen. In our case the detector consists of four quadrants, and the COM is approximated by subtracting the signal of the two sets of opposing segments. This yields the DPC vector image that relates to the in-plane electric field. Through Gauss's law and Poisson's equation, the electrostatic potential scalar image and the charge density scalar image are accessible by, respectively, integrating and differentiating the DPC vector image. Therefore, the differentiated differential phase contrast (dDPC) image represents the projected charge density and the integrated differential phase contrast (iDPC) image represents the projected electrostatic potential [43]. In comparison with standard annular bright field, DPC techniques are very good to image light elements

TABLE I. Lattice plane spacing (in angstroms) measured by STEM and XRD.

Å	R1	R2	R1 relaxed	XRD
$d(111)$	2.95–3.02	2.96–2.98	2.92–2.95	2.96
$d(11\text{-}1)$	2.91–2.93	2.87–2.92	2.93–2.95	2.93
$d(001)$	5.06–5.07	5.05–5.07	5.05–5.11	5.06

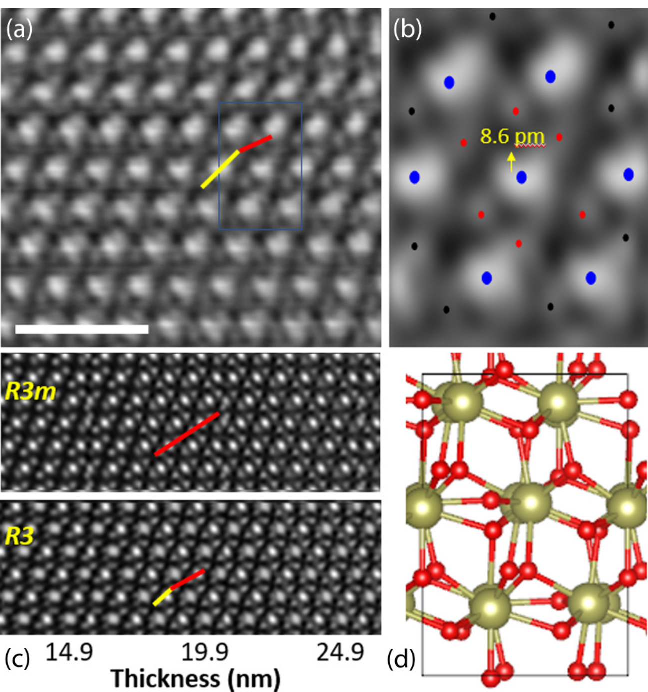

FIG. 4. (a) dDPC image of a HZO film, scale 1 nm. The blue box is enlarged in (b). The blue (red) spots represent the position of the Hf/Zr (oxygen) atoms, with an overall displacement on 8.6 pm. (c) Simulated dDPC images for the *R*3*m* and *R*3 phases. The yellow and red lines emphasize the best match between experimental data and the *R*3 phase. (d) Simulated *R*3 unit cell.

like oxygen, nitrogen, and hydrogen [44]. The differentiated DPC (dDPC) images representing the projected charge density of the specimen were simulated for *R*3 and *R*3*m* phases (structures obtained from Wei *et al.* [26]) through multislice simulations [Fig. 4(c)]. In the *R*3*m* phase, O-Hf-O//O-Hf-O columns [along the direction indicated in Fig. 4(c), top, by the red line] are collinear, whereas in the *R*3 phase, the loss of mirror symmetry results in the loss of this collinearity when observed along the [110] zone [Fig. 4(c), bottom, red and yellow lines]. In our experimental dDPC [Fig. 4(b)] also there is also no collinearity, suggesting that *R*3 is a better match for our phase than *R*3*m*. The simulated unit cell for the *R*3 phases, shown in Fig. 4(d), also shows better resemblance to the dDPC image than the *R*3*m* phase.

Next, we estimated the polarization of the *R*3 phase from our dDPC images. The position of the atomic column in one unit cell (Hf/ZrO_2) was assigned as the position corresponding to the maximum intensity of the column. These columns are overlaid on top of the image [Fig. 4(b)]. The center of mass of the cationic columns (V_c) and anionic columns (V_a) was computed across four different unit cells, and displacement ($d = V_c - V_a$) of 8.5–9 pm was measured in the [111] direction (consistent with the rhombohedral symmetry). The polarization (P_r) is then roughly estimated using the equation $P_r = qe(\frac{d}{V})$, where $q = 5$ represents the Born effective charge on the cation in HZO [45,46], $e = 1.602 \times 10^{-12}$ C, and V is the unit-cell volume ($\sim$395 Å^3), to be $1.6 - 1.9\,\mu\text{C cm}^{-2}$, pointing out of the film (along [111]).

C. Determination of the unit cell parameters

Further XRD analysis was carried out to confirm the symmetry of the bulk film and determine the lattice parameters of the cell. Considering a *R*3 lattice, (111) oriented, in-plane grazing incidence x-ray diffraction (IP-GIXRD) analysis with a large-area two-dimensional (2D) detector, of 14.8° in 2θ and 7° in γ, was carried out to access the (-220) and (-440) diffraction peaks. The (-220) peak [resp. (-440)] had a sixfold symmetry in φ and was centered around $2\theta = 50.8°$ (resp. 113.0°), which corresponds to a d spacing of $d_{\text{-}220} = 1.80$ Å (φ scans can be found in Fig. S3 in the Supplemental Material [41]). This value is in accordance with the d spacing measured with quantitative analysis of the RHEED images for the surface (1.81–1.83 Å) found for the high-symmetry direction parallel to the [11–20] axis of GaN.

Finally, off-axis measurements were carried out to measure the d spacing along the (200), the (311), and the (042) directions. Diffraction peaks with a sixfold symmetry in φ were obtained for $\chi = 55.4°$ and $2\theta = 35.4°$, indicating $d_{200} =$ 2.53 Å. Similarly, diffraction peaks with a sixfold symmetry in φ were obtained for $\chi = 30°$ and $2\theta = 60.2°$, indicating $d_{311} = 1.54$ Å. Additional diffraction peaks with a sixfold symmetry in φ were obtained for $\chi = 39.2°$ and $2\theta = 85.3°$, indicating $d_{042} = 1.14$ Å.

Assuming $d^2_{(0-11)} = d^2_{(001)} + d^2_{(010)} - 2d_{(001)}[d_{(010)}\cos(\alpha)]$, with α the rhombohedral angle, which is a valid approximation for $(90 - \alpha) < 1°$, we estimate from the values measured by STEM (see Table I) as $\alpha = 89.5 \pm 0.2°$.

Using the VESTA [47] software, the *R*3 strained cell is computed with the experimental values of $\alpha = 89.4°$ and $a \sim d_{(001)} = 5.07$ Å. The computed values of the d spacing match the experimental values of the planes observed by XRD and RHEED, as well as the angles between the measured planes and the (111) direction. The projections of the calculated unit cell are shown in Fig. S5 in the Supplemental Material [41]. The structural parameters for the *R*3 strained phase determined in this work can be found in Table S1 [41]. Along with a less rich (ony two rhombohedral domains) nanodomain structure, the rhombohedral distortion experimentally determined in this work (with a rhombohedral angle $\alpha = 89.4°$) is small compared to the *R*3*m*-phase HZO reported by Wei *et al.* [26], on perovskite electrodes: $\alpha = 88.6°$. In rhombohedral ferroelectric materials the values of P_r are directly correlated to the value of the rhombohedral angle: the lower α, the higher P_r [48]. This explains the lower polarization measured from dDPC images, in comparison to the r phase grown on perovskite electrodes.

III. CONCLUSION

By a rigorous structural analysis combining STEM, XRD, and RHEED, we demonstrated the epitaxial growth by PLD of a phase-pure rhombohedral phase of HZO on GaN (0001) belonging to the *R*3 space group and determined its lattice parameters. The found *R*3 space group (point group 3), enantiomorphic and polar, is compatible with ferroelectricity. This is a demonstration of the epitaxial growth of a polar phase of hafnium zirconate on the large-band-gap material gallium nitride.

IV. EXPERIMENTAL SECTION

An $HfZrO_4$ (HZO) target was synthesized by pressing HfO_2 and ZrO_2 powders, followed by an annealing of 4 h at 1400 °C in air. The surface of undoped GaN/Si (111) substrates was decontaminated by a dip of 30 s in HF 1% followed by a 3-min etching in HCl (36%), prior to introduction in the PLD chamber. HZO thin films of various thicknesses were grown by the pulsed laser deposition method, operating a KrF excimer laser ($\lambda = 248$ nm) at 2 Hz, with a fluence of 1.6 J cm^{-2}. The target-substrate distance was 50 mm, the substrate was heated to 750 °C, and the background gas was oxygen at a pressure of 0.1 mbar. Prior to the deposition of the HZO film, the main diffraction axes $[10\bar{1}0]$ and $[11\bar{2}0]$ of the GaN substrate were subsequently aligned with respect to a RHEED beam operating at 30 kV and photographs were taken. During the deposition, the RHEED beam was aligned with the $[10\bar{1}0]$ axis of the GaN substrate. After deposition, the films were cooled down to room temperature in the same background gas, at a ramp rate of 20 °C min^{-1}. *In situ* XPS analysis was carried out in a base pressure of 5×10^{-11} mbars, using a monochromatic Al $K\alpha$ source with a kinetic energy of 1486.7 eV, and a seven-channel analyzer.

For the symmetric XRD scans the Panalytical XPert3 Pro MRD system was used with Cu $K\alpha$ radiation ($\lambda = 1.5406$ Å) with 45 kV and 40 mA in line-focus mode. The setup included a PIXcel 3D detector on the diffracted beam side and a four-crystal Ge(220) monochromator on the incident beam side. For the IP-GIXRD measurements, a Bruker D8 Discover diffractometer was used with a rotating anode microfocus source. On the incident beam side Montel mirror optics with focused beam in the vertical direction, and a parallel beam in the horizontal direction, were used. No monochromator was used for these measurements. A 200-µm double-pinhole collimator, which reduces beam divergence to better than 6 mrad to produce a quasi point source was placed after the divergence slit. On the diffracted beam side, no secondary optics was used. The detector used was an Eiger 2R 500 K large area detector, with a range of 14.5° in 2θ and 7° in γ at a sample detector distance of 290 mm. Pole figures and subsequent pole slicing were obtained in a point focus mode.

For off-axis XRD measurements both the Bruker D8 diffractometer and the Panalytical XPert3 Pro MRD system were employed. In the MRD, the PIXcel 3D detector was used with, on the incident beam side, a 1/2° divergence slit and a 4-mm mask and no monochromator. In this system, the incident angle was changed to align the crystal planes for the diffraction measurements. In the Bruker D8, the angle χ of the sample was tilted to align the planes to measure them.

Electron transparent lamellae for STEM measurements were made through the standard focus ion-beam procedure (Thermo Fisher Helios G4 CX). The STEM measurements were conducted on a Themis Z from Thermo Fisher Inc in STEM imaging mode. HAADF-STEM images were obtained with the detector with collection angle range 65–200 mrad. dDPC images were obtained using a detector segmented in four quadrants; each span had a collection angle range of 8–30 mrad, and the contrast has been inverted for better visibility. The high tension was 300 kV and the beam convergence angle was 23.1 mrad. The measured screen current was 52 pA. Multislice image simulations of HfO_2 were performed using DR. PROBE software [49]. For the simulations the calibrated experimental values of the beam semiconvergence angle and detector collection angles were used, and all aberrations, except for defocus, were set to zero. The HfO_2 crystal was divided in four equally thick slices that each contained one atomic plane. The dDPC images were computed based on the work of Lazić *et al.* [43] The final simulated images were convolved with a two-dimensional Gaussian with a full width at half maximum of 70 pm, to account for the finite probe size.

ACKNOWLEDGMENTS

L.B.-L. acknowledges the funding received from Netherlands Organisation for Scientific Research NWO under Grant Agreement No. 718.016.002 ("TOP-PUNT"). P.N. acknowledges the funding received from the European Union's Horizon 2020 research and innovation program under Marie Sklodowska-Curie Grant Agreement No. 794954 (nickname: FERHAZ).

[1] C. Wu, P. Han, S. Liu, T. Hsieh, F. J. Lumbantoruan, Y. Ho, J. Chen, K. Yang, H. Wang, Y. Lin, P. Chang, Q. H. Luc, Y. Lin, and E. Y. Chang, IEEE Electron Device Lett. **39**, 991 (2018).

[2] G. Li, X. Li, J. Zhao, Q. Zhu, and Y. Chen, J. Mater. Chem. C **7**, 5677 (2019).

[3] D. Jena, R. Page, J. Casamento, P. Dang, J. Singhal, Z. Zhang, J. Wright, G. Khalsa, Y. Cho, and H. G. Xing, Jpn. J. Appl. Phys. **58**, SC0801 (2019).

[4] C. Lee, C. Yang, C. Tseng, J. Chang, and R. Horng, IEEE Trans. Electron Devices **62**, 2481 (2015).

[5] X. Xu, J. Zhao, G. Li, J. Xu, and X. Li, Appl. Phys. A **124**, 490 (2018).

[6] J. Zhu, L. Chen, J. Jiang, X. Lu, L. Yang, B. Hou, M. Liao, Y. Zhou, X. Ma, and Y. Hao, IEEE Electron Device Lett. **39**, 79 (2018).

[7] L. Li, Z. Liao, N. Gauquelin, M. D. Nguyen, R. J. E. Hueting, D. J. Gravesteijn, I. Lobato, E. P. Houwman, S. Lazar, J. Verbeeck, G. Koster, and G. Rijnders, Adv. Mater. Interfaces **5**, 1700921 (2018).

[8] L. Xu, X. Li, Q. Zhu, X. Xu, and M. Qin, Mater. Lett. **193**, 240 (2017).

[9] M. Coll, J. Fontcuberta, M. Althammer, M. Bibes, H. Boschker, A. Calleja, G. Cheng, M. Cuoco, R. Dittmann, B. Dkhil, I. El Baggari, M. Fanciulli, I. Fina, E. Fortunato, C. Frontera, S. Fujita, V. Garcia, S. T. B. Goennenwein, C.-G. Granqvist, and J. Grollier *et al.*, Appl. Surf. Sci. **482**, 1 (2019).

[10] E. T. Breyer, H. Mulaosmanovic, S. Slesazeck, and T. Mikolajick, in *IEEE International Symposium on Circuits and Systems (ISCAS), 2018* (IEEE, Piscataway, NJ, 2018), pp. 1–5.

[11] M.-K. Kim and J.-S. Lee, Nano Lett. **19**, 2044 (2019).

[12] T. S. Böscke, J. Müller, D. Bräuhaus, U. Schröder, and U. Böttger, Appl. Phys. Lett. **99**, 102903 (2011).

[13] M. Hyuk Park, H. Joon Kim, Y. Jin Kim, T. Moon, and C. Seong Hwang, Appl. Phys. Lett. **104**, 072901 (2014).

[14] T. Shiraishi, K. Katayama, T. Yokouchi, T. Shimizu, T. Oikawa, O. Sakata, H. Uchida, Y. Imai, T. Kiguchi, T. J. Konno, and H. Funakubo, Appl. Phys. Lett. **108**, 262904 (2016).

[15] M. Hoffmann, U. Schroeder, T. Schenk, T. Shimizu, H. Funakubo, O. Sakata, D. Pohl, M. Drescher, C. Adelmann, R. Materlik, A. Kersch, and T. Mikolajick, J. Appl. Phys. **118**, 072006 (2015).

[16] K.-T. Chen, C.-Y. Liao, C. Lo, H.-Y. Chen, G.-Y. Siang, S. Liu, S.-C. Chang, M.-H. Liao, S.-T. Chang, and M. H. Lee, in *Electron Devices Technology and Manufacturing Conference (EDTM), 2019* (IEEE, Piscataway, NJ, 2019), pp. 62–64.

[17] M. H. Park, Y. H. Lee, H. J. Kim, Y. J. Kim, T. Moon, K. D. Kim, J. Müller, A. Kersch, U. Schroeder, T. Mikolajick, and C. S. Hwang, Adv. Mater. **27**, 1811 (2015).

[18] M. H. Park, Y. H. Lee, H. J. Kim, T. Schenk, W. Lee, K. D. Kim, F. P. G. Fengler, T. Mikolajick, U. Schroeder, and C. S. Hwang, Nanoscale **9**, 9973 (2017).

[19] M. G. Kozodaev, A. G. Chernikova, R. R. Khakimov, M. H. Park, A. M. Markeev, and C. S. Hwang, Appl. Phys. Lett. **113**, 123902 (2018).

[20] M. Hyuk Park, H. Joon Kim, Y. Jin Kim, W. Lee, H. Kyeom Kim, and C. Seong Hwang, Appl. Phys. Lett. **102**, 112914 (2013).

[21] M. Hyuk Park, H. Joon Kim, Y. Jin Kim, W. Lee, T. Moon, and C. Seong Hwang, Appl. Phys. Lett. **102**, 242905 (2013).

[22] É. O'Connor, M. Halter, F. Eltes, M. Sousa, A. Kellock, S. Abel, and J. Fompeyrine, APL Mater. **6**, 121103 (2018).

[23] J. Bouaziz, P. Rojo Romeo, N. Baboux, and B. Vilquin, J. Vac. Sci. Technol. B **37**, 021203 (2019).

[24] T. Shimizu, T. Yokouchi, T. Shiraishi, T. Oikawa, P. S. S. R. Krishnan, and H. Funakubo, Jpn. J. Appl. Phys. **53**, 09PA04 (2014).

[25] S. Starschich, T. Schenk, U. Schroeder, and U. Boettger, Appl. Phys. Lett. **110**, 182905 (2017).

[26] Y. Wei, P. Nukala, M. Salverda, S. Matzen, H. J. Zhao, J. Momand, A. S. Everhardt, G. Agnus, G. R. Blake, P. Lecoeur, B. J. Kooi, J. Íñiguez, B. Dkhil, and B. Noheda, Nat. Mater. **17**, 1095 (2018).

[27] J. Lyu, I. Fina, R. Solanas, J. Fontcuberta, and F. Sánchez, ACS Appl. Electron. Mater. **1**, 220 (2019).

[28] J. Lyu, I. Fina, R. Solanas, J. Fontcuberta, and F. Sánchez, Appl. Phys. Lett. **113**, 082902 (2018).

[29] H. Y. Yoong, H. Wu, J. Zhao, H. Wang, R. Guo, J. Xiao, B. Zhang, P. Yang, S. J. Pennycook, N. Deng, X. Yan, and J. Chen, Adv. Funct. Mater. **28**, 1806037 (2018).

[30] M. Dogan, N. Gong, T.-P. Ma, and S. Ismail-Beigi, Phys. Chem. Chem. Phys. **21**, 12150 (2019).

[31] Y. Goh and S. Jeon, Nanotechnology **29**, 335201 (2018).

[32] A. Chernikova, M. Kozodaev, A. Markeev, D. Negrov, M. Spiridonov, S. Zarubin, O. Bak, P. Buragohain, H. Lu, E. Suvorova, A. Gruverman, and A. Zenkevich, ACS Appl. Mater. Interfaces **8**, 7232 (2016).

[33] J. Junquera and P. Ghosez, Nature **422**, 506 (2003).

[34] L. Baudry and J. Tournier, J. Appl. Phys. **90**, 1442 (2001).

[35] Y. Li, R. Liang, J. Wang, C. Jiang, B. Xiong, H. Liu, Z. Wang, X. Wang, Y. Pang, H. Tian, Y. Yang, and T. Ren, IEEE Electron Device Lett. **40**, 826 (2019).

[36] X. Sun, P. Wang, K. Ni, S. Datta, and S. Yu, in *IEEE International Electron Devices Meeting (IEDM), 2018* (IEEE, Piscataway, NJ, 2018), pp. 3.1.1–3.1.4.

[37] H. Mulaosmanovic, J. Ocker, S. Muller, M. Noack, J. Muller, P. Polakowski, T. Mikolajick, and S. Slesazeck, in *Symposia on VLSI Technology and Circuits, 2017* (IEEE, Piscataway, NJ, 2017), pp. T176–T177.

[38] M. Jerry, P.-Y. Chen, J. Zhang, P. Sharma, K. Ni, S. Yu, and S. Datta, in 2017 *IEEE International Electron Devices Meeting (IEDM), 2017* (IEEE, Piscataway, NJ, 2017), pp. 6.2.1–6.2.4.

[39] A. Aziz, E. T. Breyer, A. Chen, X. Chen, S. Datta, S. K. Gupta, M. Hoffmann, X. S. Hu, A. Ionescu, M. Jerry, T. Mikolajick, H. Mulaosmanovic, K. Ni, M. Niemier, I. O'Connor, A. Saha, S. Slesazeck, S. K. Thirumala, and X. Yin, in *Design, Automation and Test in Europe Conference and Exhibition (DATE), 2018* (IEEE, Piscataway, NJ, 2018), pp. 1289–1298.

[40] L. Chen, T.-Y. Wang, Y.-W. Dai, M.-Y. Cha, H. Zhu, Q.-Q. Sun, S.-J. Ding, P. Zhou, L. Chua, and D. W. Zhang, Nanoscale **10**, 15826 (2018).

[41] See Supplemental Material at http://link.aps.org/supplemental/10.1103/PhysRevMaterials.4.043401 for AFM topography images, HAADF-STEM EELS maps of the film, XRD data, and representation and structure parameters of the *R*3 unit cell of the grown film.

[42] D. Pesquera, X. Marti, V. Holy, R. Bachelet, G. Herranz, and J. Fontcuberta, Appl. Phys. Lett. **99**, 221901 (2011).

[43] I. Lazić, E. G. T. Bosch, and S. Lazar, Ultramicroscopy **160**, 265 (2016).

[44] S. de Graaf, J. Momand, C. Mitterbauer, S. Lazar, and B. J. Kooi, Sci. Adv. **6**, eaay4312 (2020).

[45] R. Materlik, C. Künneth, and A. Kersch, J. Appl. Phys. **117**, 134109 (2015).

[46] P. Fan, Y. K. Zhang, Q. Yang, J. Jiang, L. M. Jiang, M. Liao, and Y. C. Zhou, J. Phys. Chem. C **123**, 21743 (2019).

[47] K. Momma and F. Izumi, J. Appl. Crystallogr. **44**, 1272 (2011).

[48] N. W. Thomas and A. Beitollahi, Acta Crystallogr. B **50**, 549 (1994).

[49] J. Barthel, Ultramicroscopy **193**, 1 (2018).